Segmentation and Visualization of Dynamic Cardiac Vessels and Adjusted Quantification of Related Flow Parameters

Category: Application

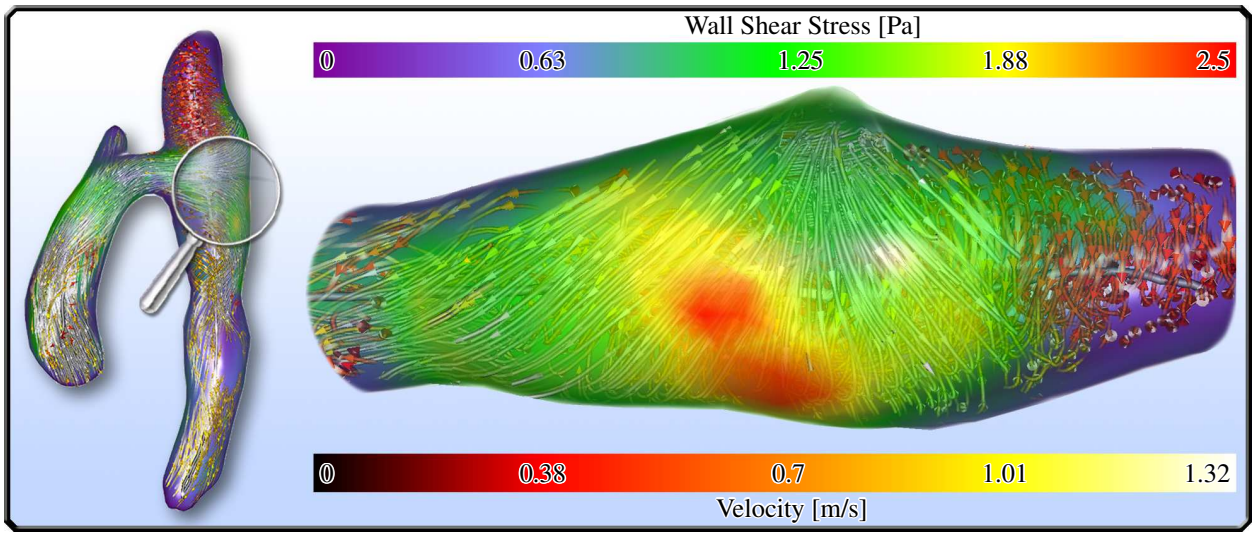

Fig. 1. High velocity blood flow passes the aortic arch and impinges on the vascular wall. The emerging vortex flow caused increased wall shear stress for more than a decade and promoted a pathologic dilation of the patient's left subclavian artery (above the magnifier).

Abstract— Cardiovascular diseases (CVDs) are the leading cause of death worldwide. In recent years, 4D PC-MRI acquisitions gained increasing importance. They enable the non-invasive and reliable measuring of time-resolved three-dimensional flow data that allow the qualitative and quantitative evaluation of patient-specific hemodynamics. The quantification of parameters like wall shear stress and stroke volumes is essential to comprehend the genesis and evolution of different cardiac pathologies. Their accurate assessment is dependent on the wall position and vessel diameter, respectively. Time-varying segmentation of the cardiac morphology is a complex task that has been realized from an image processing point of view using techniques like graph cuts and deformable models. Yet, current works in the field of medical visualization and quantification rely on a static three-dimensional vessel approximation and thus introduce calculation errors. In this work, we present a full processing pipeline including a graph cut-based four-dimensional segmentation and a smooth but accurate visualization of the obtained time-dependent vessel surface. We incorporate the results to adjust the quantification, investigate the deviation to the non-dynamic approach and evaluate datasets with different pathologies like aneurysms and coarctations. In collaboration with cardiologists and radiologists we discuss the capability of our approach to complement available diagnosis information and how treatment decisions are affected.

Index Terms—4D pc-mri, cardiac blood flow, 4D segmentation, cardiac motion visualization, quantification, wall shear stress.

1 Introduction

As determined by the World Health Organization, cardiovascular diseases (CVDs) are the leading cause of death worldwide [30]. The evaluation of a patient's status and prediction of disease progression requires consideration of diverse variables. Recent research suggests that vortex flow as qualitative parameter is a strong indication for the presence of several pathologies [5]. On the other hand, quantitative measures support the comprehension about the initiation and progression of diseases. Stroke volumes – the amount of pumped blood per heartbeat – help to assess the patient's cardiac function, whereas wall shear stress is associated with aneurysm formation, growth and rupture [9]. With our work, we contribute to an improved determination of those measures and, hence, support the diagnosis and treatment planning for several pathologic conditions of the vascular system.

In the past years, four-dimensional phase-contrast magnetic resonance imaging (4D PC-MRI) gained importance. It is a young non-invasive image modality that allows spatial and time-resolved qualitative and quantitative insight into the hemodynamics [26, 28]. 4D PC-MRI helps to investigate the individual pathophysiology, disease progression and outcome. Due to the huge amount and complexity of the four-dimensional data, the common standard in medical applications is to employ a static three-dimensional approximation of the time-dependent vessel wall. Thus, an easier and faster preprocessing is traded for information about the heart's cyclic movement. However, the precise definition of temporal hemodynamics in vessels requires determination of wall position, orientation and the vessel diameter during the cardiac cycle. As a consequence, an approach which neglects these components is error-prone. The creation of guided techniques is necessary to overcome these issues and improve reliability of 4D PC-MRI in the clinical setting [28]. This may result in lower inter-observer variability. Furthermore, an enhanced level of automatization will speed up data processing and thus enable larger studies.

The extraction of time-dependent segmentations is a common issue and has been worked on by several approaches from the image processing community. Unfortunately, the subsequent surface extraction, dynamic visualization and utilization of the results to adjust the quantification of medical parameters is no focus of such works.

Medical applications benefit greatly by taking advantage of the user's expert knowledge. Graph cuts are a common segmentation tech-

nique for the medical context [7, 25]. Where other approaches go beyond the expertise of medical doctors, they require the specification of areas inside and outside the target structure. Hence, the character of user input fits well to the mental model and experiences of clinicians.

In this paper, we present a guided procedure to obtain movement information mainly of the aorta and pulmonary artery. First, the user creates a three-dimensional segmentation assisted by the graph cut technique. From this base segmentation we calculate segmentations of all temporal positions using an adapted graph cut. The input is set automatically, but can repeatedly be adjusted as desired to exploit the experts' knowledge. A vectorial displacement list per vertex is derived by projecting the triangular surface mesh extracted from the base segmentation onto the meshes of each temporal position. We apply two postprocessing steps and put additional effort in realizing a smooth and precise visualization of the cyclic cardiac movement. The resulting information are employed to adjust the calculation of vectorial wall shear stress and the stroke volume. To the best of our knowledge, there is no other work that takes the dynamic morphology into account for the calculation of quantitative measures in the heart. Summarizing, the main contributions of this paper are:

- We describe a model for the dynamic vessel morphology based on a displacement list per vertex.
- We provide a guided graph cut-based workflow to obtain vessel segmentations in all temporal positions.
- We realize a smooth but accurate visualization of the heart's movement.
- We adjust the quantification of vectorial wall shear stress and stroke volume to the motion information and investigate the deviations between the conventional and motion-aware calculation.

In Section 2, we provide basic information about 4D PC-MRI and related wall shear stress quantification. Additionally, we give an overview of common visualization techniques for blood flow data as well as time-dependent cardiac segmentation and visualization approaches. Section 3 continues with details about selected cardiac diseases and information about data acquisition and preprocessing. After the requirement analysis in Section 4, we proceed with the segmentation and visualization of the cardiac motion as well as the adjusted quantification of wall shear stress and stroke volume in Section 5. We apply our method to different patient datasets in Section 6 and draw conclusions in Section 7.

2 Related Work

4D PC-MRI Four-dimensional phase-contrast magnetic resonance imaging has the potential to become the leading image modality to assess the cardiac hemodynamics. The measured data show good agreement with the common 2D PC-MRI [39] and allow a more flexible data analysis. Markl et al. [28] and Lotz et al. [26] provide an overview of common 4D PC-MRI techniques. Hennemuth et al. [17] describe a pipeline for interactive data exploration including preprocessing.

Visualization of Blood Flow Data: The high complexity of the time-resolved three-dimensional flow data leads to heavy visual clutter. Thus, a variety of exploration approaches and expressive visualizations were introduced that help to get better insight into the patient's hemodynamics. Examples are illustrative techniques like speed lines by van Pelt et al. [45] and Born et. al [6], the FlowLens by Gasteiger et al. [14] and anatomy-guided exploration by Neugebauer et al. [32]. The line predicates technique was introduced by Salzbrunn et al. [41] and used to extract qualitative flow features like vortices [5, 21]. Pobitzer et al. [36] describe a method to minimize the number of pathlines necessary to cover the spatio-temporal dataset domain. McLoughlin et al. [29] provide an overview of common flow visualization techniques.

Wall Shear Stress Quantification in 4D PC-MRI Data: The quantification of parameters like stroke volumes support the assessment of the cardiac functionality, whereas other measures like wall shear stress help to understand and predict the evolution of pathologies. Papaioannou et al. [34] provide an overview about wall shear stress calculations in blood vessels. Potters et al. [38] and Ooij et al. [43] describe a method to determine the vectorial aortic wall shear stress in 4D PC-MRI data. Several works [23, 37] point out the sensitivity to even small changes in the wall geometry and the spatial resolution of the data. Computational fluid dynamics (CFD) simulations were used to validate the results [35]. Castro et al. [9] estimated the motion of intracranial aneurysms from four-dimensional computerized tomography images, simulated the flow in all temporal positions and compared the wall shear stress distributions. In the field of cerebral aneurysms, there is an ongoing discussion about the role of high and low wall shear stress concerning the risk of rupture [33].

Four-Dimensional Cardiac Segmentation: Graph cuts were introduced by Boykov et al. [8] and have successfully been used to obtain spatio-temporal segmentations of the heart [10, 25, 27]. Since a naive implementation is computationally expensive, methods were developed that exploit parallelism [24] and employ special data structures to increase cache efficiency [20]. Other works use level sets [13, 49] or deformable models [1, 31] to extract time-dependent segmentations of the heart. Bertram et al. [4] put emphasis on the extraction of fair triangular surfaces from already given four-dimensional segmentations.

Visualization of the Cardiac Movement: To the best of our knowledge, approaches that visualize the cardiac motion with explicit surface representations are rare. Instead, several works [46, 48] use GPU-accelerated time-varying direct volume rendering to display the measured anatomical data. Cine MRI is another common technique that acquires a series of slice images throughout the cardiac cycle, which are then presented as movie.

3 Medical Background

There is a large number of highly diverse cardiovascular diseases [30]. Recent developments of 4D PC-MRI enable the time-resolved three-dimensional assessment of patient-specific information about vessel hemodynamics. The obtained information help to comprehend the nature of pathologies and determine correlations between different aspects.

3.1 Cardiovascular Vortex Flow

Normal flow in the great vessels is typically laminar and displays an approximate parabolic velocity profile with the highest velocity in the center of the vessel. Valvular and vascular pathologies have been shown to disrupt this normal flow pattern, resulting in turbulent flow. A classic flow turbulence is the so called vortex flow pattern. In the following, we explain selected pathologies causing vortex flow. For further information we refer to [21].

Vascular Diameter Alterations: Both dilatation and narrowing of vessels will result in altered flow dynamics. Slight dilations up to a factor of 1.5 are called ectasia, above they are referred to as an aneurysm. In contrast, coarctation of the aortic arch is defined as an abnormal narrowing of the aorta. In all cases, the altered vessel shape promotes the formation of vortex flow in the corresponding vessel sections.

Marfan Syndrome: The Marfan Syndrome is an inherited connective tissue disorder which leads to vessel dilatation and hence is associated with increased vortex flow in the ascending aorta compared to healthy volunteers [16]. Such patients are susceptible to ectasia and aneurysm development.

Valve Pathologies: Valve defects can be treated by implanting an artificial valve. Valve replacements are performed for stenosis (an abnormal narrowing of a heart valve) or insufficiency (an abnormal amount of retrograde flow that severely affects the cardiac function negatively). Yet, heart surgery is invasive and should only be performed when a positive benefit-risk ratio is likely.

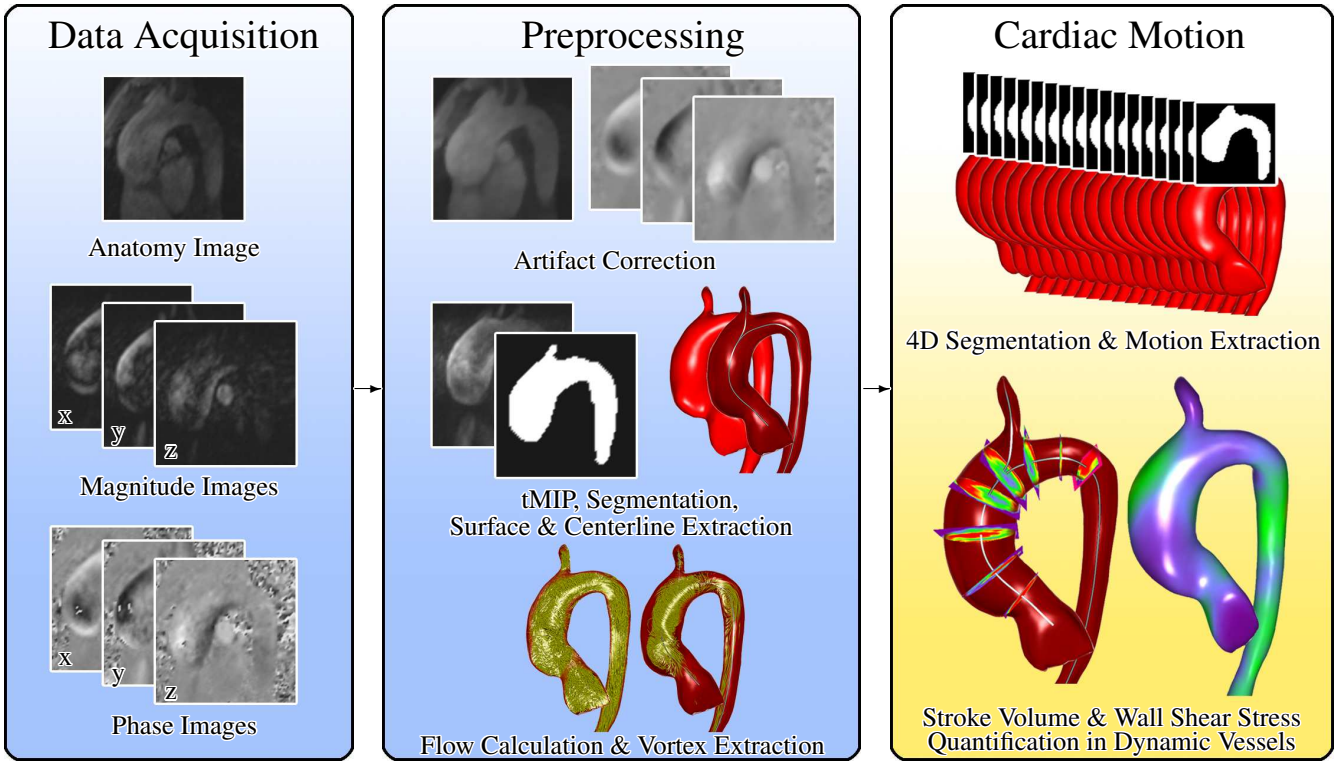

(a) (b) (c)

Fig. 2. Data acquisition, preprocessing and motion extraction pipeline. (a) A 4D PC-MRI data acquisition provides an anatomy image as well as each three magnitude and phase images that represent the flow strength and direction, respectively. (b) The preprocessing includes artifact correction in the anatomy and phase images as well as the calculation of a temporal maximum intensity projection (tMIP) of the magnitude images. The performed three-dimensional segmentation is used to extract a triangular surface mesh plus its centerline. The full flow is integrated and vortices are extracted. (c) The calculation of a four-dimensional segmentation is used to obtain the cardiac motion. The stroke volume and wall shear stress quantification is adjusted to the dynamic vessel.

Bicuspid Aortic Valve: The aortic valve is located between the left ventricle and the aorta. In healthy humans, the valve consists of three leaflets. It opens during the systole, when oxygenated blood is pumped into the body, and closes during the diastole to prevent blood from flowing back into the left ventricle. The term bicuspid aortic valve (BAV) is used if the valve consists of only two leaflets. In this setting the physiological laminar flow is disturbed and vortex flow in the ascending aorta during the systole is generated [18].

3.2 The Role of Wall Shear Stress

Wall shear stress (WSS) is the force on the inner layer of the vessel caused by flowing blood. WSS has been shown to be associated with vortex flow close to the vessel wall. A significantly increased WSS was detected in the ascending aortas of BAV patients [44]. Recent research suggests that the presence of high shear forces over a long period of time promotes vessel dilations [9]. From a clinical standpoint this is interesting as aortic aneurysms above a certain diameter bear the risk of rupture, which is lethal in most of the cases. Thus, an estimation of the risk level of aneurysm development and rupture by evaluating vortex flow-induced high shear forces has the potential to guide therapeutic decisions in the future. If the rupture risk is high, replacement of the aortic valve and ascending aorta has to be considered as a prevention of potentially lethal consequences.

3.3 Data Acquisition and Preprocessing

A 3T Siemens Verio MR scanner was used for the data acquisition with a maximal expected velocity parameter (V_{ENC}) of 1.5 m/s. A scan consists of seven components: a T1-weighted image provides information about the patient-specific anatomy. Each three phase and magnitude images for x-, y- and z-dimension describe the flow direction and strength, respectively. The obtained spatial resolution is 1.77 mm^2 in a 132×192 grid inplane with a distance of 3.5 mm for each of the 15 to 23 slices. The temporal resolution varies from 14 to 21 time steps with about 50 ms difference between each temporal position. Figure 2a illustrates the acquired data. For artifact reduction the phase images were preprocessed using an eddy current correction [22] and a phase unwrapping algorithm [11].

Vessel Segmentation: First, the maximum intensity projection over time (tMIP) of the magnitude images is calculated. The resulting high contrast image is employed to perform a three-dimensional graph cut with a 26-neighborhood per voxel[1] [8, 20, 24]. Gradients $G_{\{x,y,z\}}$ in the $[0,1]$-scaled tMIP are calculated via finite differences. An exponential function is used to specify weights w between the graph nodes:

$$w = \exp\left(-\alpha \cdot G^2_{\{x,y,z\}}\right) \quad (1)$$

The higher the tolerance parameter α is, the larger the segmented region becomes. $\alpha = 1000$ is used as an experimentally determined default value. The required graph cut input – the specification of regions inside and outside the vessel – is user-given. Each inside-voxel is connected to the first terminal node, each outside-node to the second one. All edge weights to terminal nodes are set infinite. The resulting three-dimensional segmentation is postprocessed using the $3 \times 3 \times 3$ sized morphological operators closing and opening.

Initial Surface Reconstruction: Marching cubes is employed to extract a triangular surface mesh from the segmentation. The mesh is

[1] GridGraph_3D_26C (GridCut)

smoothed using a low-pass filter [42] and reduced via quadric decimation [19]. Afterwards, the centerlines are extracted[2] [3].

Flow Calculation: The GPU is utilized to integrate the full set of pathlines [36] via adaptive step size Runge-Kutta-4 [12] and to derive the λ_2 vortex criterion that is required for the line predicate-based vortex extraction [21]. Velocity vectors $\vec{u} = (u,v,w)^{\mathrm{T}}$ in the four-dimensional flow field $\mathbb{V}$ at the spatio-temporal position $\vec{x} = (x,y,z,t)^{\mathrm{T}}$ are obtained using quadrilinear interpolation. The temporally adjacent vectors $\vec{u_{\lfloor t \rfloor}} = \mathbb{V}(x,y,z,\lfloor t \rfloor)$ and $\vec{u_{\lceil t \rceil}} = \mathbb{V}(x,y,z,\lceil t \rceil)$, both obtained via hardware-accelerated trilinear interpolation, are used to perform a last linear interpolation manually. Figure 2b depicts the preprocessing steps.

For flow visualization, common techniques like illuminated streamlines emphasized with halos [29] are utilized. Pathlines are color-coded by velocity – de facto a standard in radiology in particular due to the widespread use in Doppler ultrasound. A ghosted view technique [15] shows parts of the cut away vessel front. In the animation mode, particles with trails [45] are shown. Order-independent transparency is implemented on the GPU [47] to ensure correct alpha blending.

4 Requirement Analysis

Achieving a real-time capable visualization of the heart's motion requires the usage of the GPU's potential. Thus, an appropriate mesh model has to be created that fits the OpenGL shader pipeline. In addition, the model has to be flexible enough to capture the potentially altered pathologic vessel morphologies.

A smooth but accurate visualization of the cardiac motion is required. Therefore, the transition between subsequent heartbeats of the cyclic movement needs special attention and intelligent noise removal is inevitable.

A moving vessel entails the adjustment of other components in the framework. Centerlines become time-dependent and protruding pathlines due to the vessel contraction have to be masked. Planes orthogonal to the centerline are used to quantify stroke volumes. It must be ensured that they fit the vessel at any time and stay perpendicular to the now dynamic centerline.

The time-varying extent and orientation of the planes has to be considered for the stroke volume calculation, whereas the WSS quantification has to take the wall motion into account.

The applicability of our method for clinical routine depends on the provision of well-reasoned default values especially for unintuitive parameters. Ease of use has to be ensured by fitting the remaining input into the users' mental model by using parameters that relate to anatomical or cardiologic knowledge.

5 Segmentation and Visualization of the Cardiac Motion and Quantification Adjustment

In this section, we present our method to extract and visualize the cardiac motion as well as the necessary steps to adjust the WSS and stroke volume quantification.

5.1 Cardiac Motion

In the following, we provide explanations about the extraction of the heart's motion. We start with the creation of an appropriate surface mesh model and proceed with the necessary steps to obtain the movement information, which includes a four-dimensional vessel segmentation. A description of the smooth but accurate real-time motion visualization and the adjustment of quantification planes and centerlines follows. Finally, we describe the modification of the WSS and stroke volume calculations to the cardiac motion.

Dynamic Mesh Model: Since the developed framework uses OpenGL, it is convenient to make use of the shader pipeline in order to exploit the GPU's computation power and establish a real-time capable motion visualization. Following this, a conventional three-dimensional triangular surface mesh M with a constant topology is used as basis, extracted from the segmentation performed on the magnitude tMIP. Every vertex $v \in M$ stores a list of T three-dimensional vectors $\vec{d_i},\ i \in [0,\ T-1]\,,\ i \in \mathbb{N}$, in the following referred to as displacements. T is the number of temporal positions in the dataset. The vertex shader receives the current time $t \in [0,\ T-1]\,,\ t \in \mathbb{R}$ in the cardiac cycle as well as the displacements and interpolates the translated position v_{dspl} from the temporally adjacent displacements $\vec{d_{\lfloor t \rfloor}}$ and $\vec{d_{\lceil t \rceil}}$:

$$v_{\mathrm{dspl}} = v + \left((1-\alpha)\cdot\vec{d_{\lfloor t \rfloor}} + \alpha\cdot\vec{d_{\lceil t \rceil}}\right) \quad \text{with} \quad \alpha = |t - \lfloor t \rfloor| \qquad (2)$$

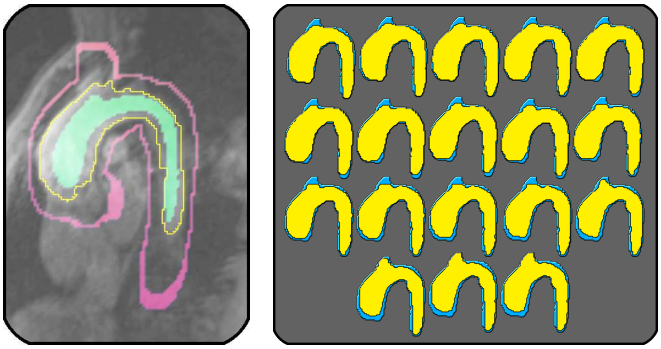

(a) (b)

Fig. 3. (a) The automatically specified graph cut setup. The green and red voxels are marked as inside and outside the vessel, respectively. The resulting segmentation is shown as yellow contour. (b) The segmentations (yellow) of this slice for all 18 temporal positions in the dataset from t_0 (top left) to t_{17} (bottom right) with the magnitude tMIP segmentation (blue) in the background as reference.

Displacement Vectors: The cardiac motion is determined from triangular meshes M_i for all temporal positions extracted from the corresponding segmentations. A displacement $\vec{d_i},\ i \in [0,\ T-1]$ for one of the T temporal positions is calculated as projection of a base mesh vertex $v \in M$ onto M_i. To do so, the closest vertex $v_i \in M_i$ to v is determined[3]. Then, a ray-triangle intersection test is performed [2] for every triangle v_i is part of. Since the base mesh M was derived from the magnitude tMIP, it is an upper boundary, i.e., the vessel is never larger than this. Consequently, the ray direction is the inward-pointing normal of the corresponding triangle. The displacement vector $\vec{d_i}$ results from the difference between v and the closest projection.

Four-Dimensional Vessel Segmentation: The manual vessel segmentation in every temporal position is a tedious, exhausting and unacceptable task that needs to be supported. The graph cut technique requires the specification of regions inside and outside the vessel as input and thus meets the requirement of fitting into the users' – in this case physicians and radiologists – mental model. Therefore, graph cuts are utilized to support the four-dimensional segmentation. The extraction task is still complex and time-consuming. For this reason, a result that can be refined if necessary, is automatically extracted as described in the following.

The time-resolved anatomy image is employed to perform the segmentation. Since the magnitude tMIP segmentation represents the maximum vessel extent, it is reasonable to assume that voxels outside the segmentation are also outside the segmentation of each temporal position. Yet, a certain safety margin seems appropriate due to possible inaccuracies in the segmentation. Therefore, two additional masks are obtained by subsequently dilating the magnitude tMIP segmentation with kernel sizes of five and three. The difference of these two masks is initialized as outside region. The result is a dilated vessel

[2] vtkMarchingCubes, vtkWindowedSincPolyDataFilter, vtkQuadricDecimation (VTK) and vmtkcenterlines (VMTK)

[3] KDTree adapted from Numerical Recipes [40]

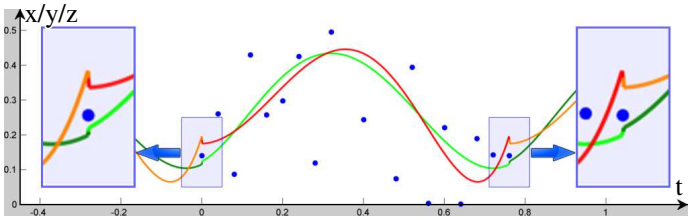

Fig. 4. A least-squares-fitted polynomial of degree 5 to the x-, y- or z-dimension of one vertex' displacement list with (dark green / green) and without (orange / red) additional conditions for C^2-continuity. A smoother transition between single heartbeats (blue rectangles) is achieved.

hull. Based on discussions with radiologists, the reasonable assumption is made that the diameter of the contracted vessel is not less than half of its maximum diameter. Following this, all voxels are specified as inside the vessel that are closer to the centerline than to the base mesh.

The initialization is equal for all temporal positions and the three-dimensional graph cut is performed separately for every temporal position. The graph cut tolerance parameter α is increased by a factor of ten to handle the noisy image data. The obtained segmentations and subsequently extracted meshes are postprocessed in the same manner as described in Section 3.3. Figure 3a shows the automatically specified outside (red) and inside voxels (green) as well as the resulting segmentation (yellow contour). Figure 3b shows the segmentation of this slice (yellow) for each temporal position. The magnitude tMIP segmentation (blue) is underlaid as a reference.

Displacement Postprocessing: Each vertex v of the base mesh M stores a list of T displacement vectors $\vec{d}_i = (x_i,\ y_i,\ z_i)^{\mathrm{T}},\ i \in [0,\ T-1],\ i \in \mathbb{N}$ that describe the translation of v at the temporal positions i. For noise reduction, two postprocessing steps are applied.

The first one considers the time-dependent displacement list of each vertex separately. Three approximating polynomials are calculated – each one for the x-, y- and z-dimension. Their degree m must provide enough flexibility to model the sinus movement of the heart as well as the movement in the tangential plane, but the overfitting of noise has to be avoided. The default value $m = 5$ was derived from experiments and used for all results in this work. An approximating polynomial is obtained by calculating a least squares solution[4] to the linear system $Ax = b$, where A is a Vandermonde matrix [40]:

$$A = \begin{bmatrix} x_0^m & \dots & x_0^2 & x_0 & 1 \\ x_1^m & \dots & x_1^2 & x_1 & 1 \\ \vdots & \vdots & \vdots & \vdots & \vdots \\ x_i^m & \dots & x_i^2 & x_i & 1 \\ \vdots & \vdots & \vdots & \vdots & \vdots \\ x_{T-1}^m & \dots & x_{T-1}^2 & x_{T-1} & 1 \end{bmatrix}$$

$$\text{and} \quad b = \Big(f(x_0),\ f(x_1),\ \dots\ ,\ f(x_i),\ \dots\ ,\ f(x_{T-1}) \Big)^{\mathrm{T}} \tag{3}$$

Unlike the cardiac motion, the polynomial is not periodic. This causes a step in the function at the transition between single heartbeats that leads to a bumpy animation. As a remedy, six conditions for C^2-continuity are added:

$$\begin{aligned} f(x_0) - f(x_{T-1}) = 0 \quad &\text{and} \quad f(x_{T-1}) - f(x_0) = 0, \\ f'(x_0) - f'(x_{T-1}) = 0 \quad &\text{and} \quad f'(x_{T-1}) - f'(x_0) = 0, \\ f''(x_0) - f''(x_{T-1}) = 0 \quad &\text{and} \quad f''(x_{T-1}) - f''(x_0) = 0 \end{aligned} \tag{4}$$

This leads to the adjusted linear system $A_C x = b_C$ with:

$$b_C = \Big(b,\ 0,\ \dots\ ,0 \Big)^{\mathrm{T}} \quad \text{and} \quad A_C = \begin{bmatrix} A \\ C \end{bmatrix}, \text{where} \tag{5}$$

[4] JacobiSVD with FullPivHouseholderQRPreconditioner (Eigen)

$$C = \begin{bmatrix} x_0^m - x_{T-1}^m & \dots & x_0^2 - x_{T-1}^2 & x_0 - x_{T-1} & 0 \\ x_{T-1}^m - x_0^m & \dots & x_{T-1}^2 - x_0^2 & x_{T-1} - x_0 & 0 \\ m\left(x_0^{m-1} - x_{T-1}^{m-1}\right) & \dots & 2(x_0 - x_{T-1}) & 0 & 0 \\ m\left(x_{T-1}^{m-1} - x_0^{m-1}\right) & \dots & 2(x_{T-1} - x_0) & 0 & 0 \\ m(m-1)\left(x_0^{m-2} - x_{T-1}^{m-2}\right) & \dots & 0 & 0 & 0 \\ m(m-1)\left(x_{T-1}^{m-2} - x_0^{m-2}\right) & \dots & 0 & 0 & 0 \end{bmatrix}$$

Since the system is solved in a least squares sense, the additional conditions are minimized, but no actual C^2-continuity is achieved. Nevertheless, the result quality improves significantly in terms of smoother transitions between the cardiac cycles. Figure 4 shows an approximating polynomial of degree $m = 5$ with (green / dark green) and without (red / orange) the additional conditions. The blue rectangles mark the transitions.

The second postprocessing is based on a Laplacian mesh smoothing. Every temporal position is processed separately under consideration of the topology. A displacement $\vec{d}_i^{\,v}$ of vertex v at the temporal position i is interpolated linearly in I iterations with the mean displacement $\overline{d_i^N}$ of N direct neighbors with a relaxation factor $r \in [0,\ 1]$:

$$\vec{d}_i^{\,v} = \vec{d}_i^{\,v} + r \cdot \overline{d_i^N} = \vec{d}_i^{\,v} + \frac{r}{N} \cdot \sum_{n=0}^{N-1} \vec{d}_i^{\,v_n} \tag{6}$$

$I = 250$ and $r = 0.01$ were derived as default values from experimental results. Figure 5 shows an example of one temporal position with (right) and without (left) postprocessing. The surface is color-coded according to the displacement vectors illustrated as white lines.

Motion Visualization: The motion visualization is realized within the OpenGL shader pipeline. A base mesh vertex v is passed to the vertex shader with its position, normal $\vec{n}_v$ and an index. Additional information are uploaded to the GPU as shader storage buffer object (SSBO_1). SSBO_1 contains:

- a list of all triangles,
- the number of triangles a vertex is part of,
- the corresponding triangle indices
- and the displacements per vertex.

The vertex shader receives the current temporal position of the heart cycle and interpolates the displacement as described in the previous

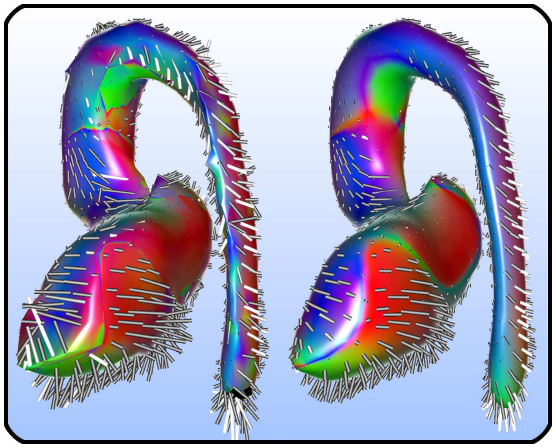

Fig. 5. Displacement vectors of one temporal position without (left) and with (right) noise reduction. The surface is color-coded according to the obtained directions that are displayed as white lines. Anatomical information are provided in Figure 7.

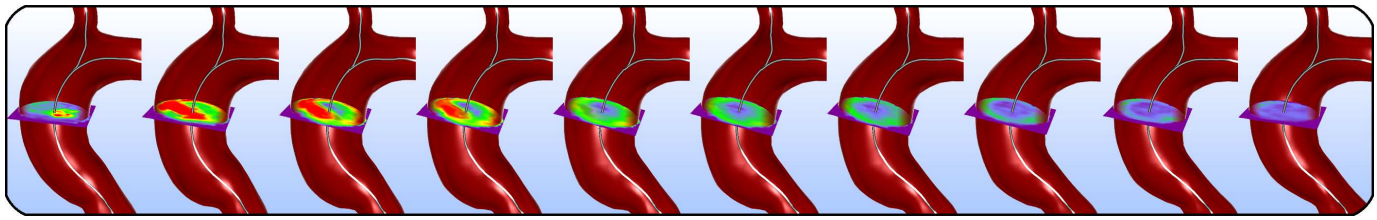

Fig. 6. The quantification plane remains orthogonal to the centerline and fits the vessel diameter at any time of the cardiac cycle. 10 of the 18 temporal positions in this dataset are shown. The color is coded according to the length of velocity vectors sampled at the corresponding positions in the plane.

Dynamic Mesh Model paragraph. The resulting position v_{dspl} is written to another SSBO_2. In the next step, the geometry shader iterates through all triangles the vertex v is part of, obtains the shifted positions from SSBO_2 and calculates normal vectors via cross products. To ensure that the normals point in the correct direction, they are compared with the corresponding base mesh normal $\vec{n_v}$ and flipped if necessary. Then, the normal of the shifted vertex is averaged from the just obtained surrounding triangle normals weighted by the distance of each corresponding triangle center to v. The subsequent fragment shader uses the normal to perform Phong illumination.

There are about 20 temporal positions in the dataset. Consequently, a displacement list merely contains about 20 vectors. Linear interpolation of these few samples will not lead to a fluent motion visualization. Therefore, one-dimensional interpolating periodic cubic b-splines with natural boundary conditions are fitted[5] to the x-, y- and z-dimension of the displacements and used to increase the number of samples by a factor of ten. Figure 7 shows a result of the motion visualization.

Framework Adaption: A time-varying vessel entails the extraction of a time-dependent centerline. In each temporal state M_i, $i \in [0,\ T-1]$, $i \in \mathbb{N}$ of the mesh, resulting from the simultaneous application of all displacements $\vec{d_i}$ to the corresponding vertices, the closest point to the base mesh centerline's start- and endpoint, respectively, is determined. Subsequently, they are used to calculate the centerline[6] C_i at temporal position i. The centerline's motion is modeled, obtained and visualized in the same way as the dynamic vessel mesh. Solely the projections are performed onto line segments instead of triangles.

[5] spline1dbuildcubic (ALGLIB)
[6] vmtkcenterlines (VMTK)

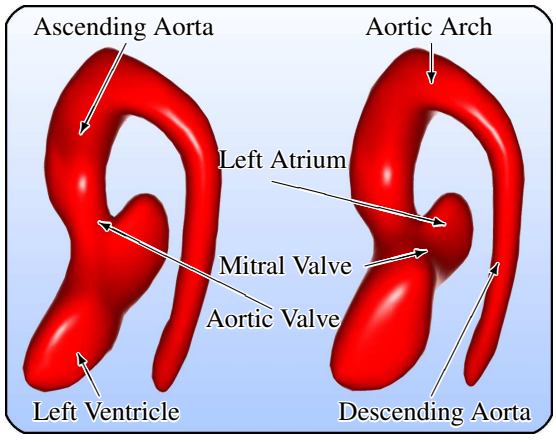

Fig. 7. Result of the cardiac motion visualization. The left ventricle contracts during the systole (left) to pump blood into the body. In the meantime, the left atrium fills and then supplies the left ventricle with new oxygenated blood during the diastole (right). Notice the increased diameter of the blood-filled descending aorta in the systole.

Planes orthogonal to the centerline are de facto a standard to quantify measures like stroke volumes. Such measures are calculated for one plane at once that is freely movable along the centerline. In our framework, a plane is modeled as 100×100 grid with a specific scale per cell and is orthogonal to a normal vector starting from a certain position. The scale is adjusted automatically to fit the vessel diameter at the corresponding position. To ensure that a plane remains perpendicular to moving the centerline and fits the vessel at every temporal position, its position, normal and scale are represented by a list of size T. The positions and normals are derived from the temporal centerline states C_i, the scales are determined separately for each temporal mesh state M_i. The lists are uploaded to the GPU as shader storage buffer object and used to span the plane in the geometry shader. The position, normal and scale at the current time $t \in [0,\ T-1], t \in \mathbb{R}$ of the cardiac cycle are obtained using linear interpolation between the two temporally adjacent list entries. Figure 6 shows an adjusted quantification plane that fits the vessel at any time and stays orthogonal to the centerline.

The flow was calculated within the magnitude tMIP segmentation. Now, when the time-varying vessel contracts, some of the pathlines will protrude. To prevent this, the stencil buffer is filled while rendering the vessel mesh and subsequently used to mask the pathlines. Cropping the actual pathline data to the four-dimensional segmentation would deprive the user of the possibility to flexibly switch the cardiac motion on and off without missing parts of the flow in the non-moving version.

5.2 Motion-Aware Quantification

In the following, we describe the WSS and stroke volume quantification as well as the necessary steps to adjust the calculations to the cardiac motion, illustrated in Figure 2c.

Wall Shear Stress: WSS is given in Pascal (Pa) and represents the force tangential to the vessel wall caused by nearby complex blood flow. It is defined as:

$$\text{WSS} = \mu\ ||\vec{\tau_{WSS}}|| \quad \text{with} \quad \vec{\tau_{WSS}} = \frac{\partial \vec{u}}{\partial \vec{n}}\,, \tag{7}$$

where $\vec{u}$ and $\vec{n}$ are the velocity and normal vectors, respectively. The blood viscosity μ is measured in centipoise (cP) and describes the resistance to gradual deformation by shear stress.

The employed WSS calculation is based on [38]. For each vertex, 20 velocity vectors are sampled along the inward-pointing normal over a distance of 0.6 mm [43]. An orthonormal basis $\{\vec{n},\ \vec{n_x},\ \vec{n_y}\}$ is created and used to obtain two-dimensional projections of the velocity vectors $\vec{u_{\text{tp}}}$ into the normal's tangential plane:

$$\vec{u_{\text{tp}}} = \begin{pmatrix} \vec{u} \cdot \vec{n_x} \\ \vec{u} \cdot \vec{n_y} \end{pmatrix} \tag{8}$$

Next, one-dimensional interpolating cubic b-splines with natural boundary conditions are fitted[5] to the list of x- and y-components of all $\vec{u_{\text{tp}}}$. The splines are used to analytically calculate the first derivative $\vec{\tau_{WSS}}$ on the vessel wall. The blood viscosity is set to 3.5 cP – a commonly made assumption for large arteries [34]. The obtained

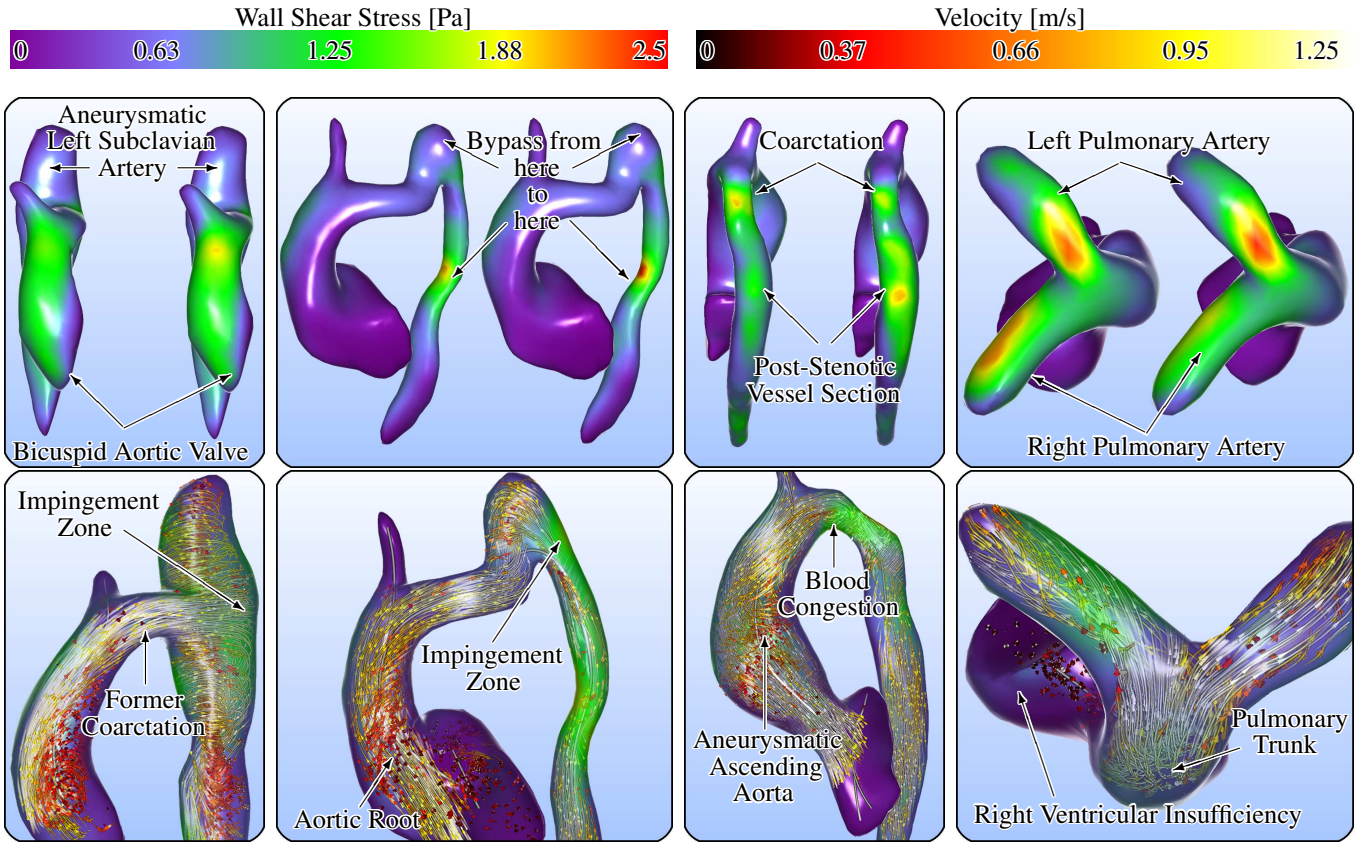

Fig. 8. Top row: WSS quantification without (each left) and with (each right) consideration of the cardiac motion. Bottom row: integrated flow visualization. All images were captured during systole. (a) Near-wall vortex flow causes high shear forces in the patient's ascending aorta. Motion-adjusted quantification produces 25% higher peak values. High velocity blood flow impinges after passing the former coarctation and exposes the wall to increased shear forces. (b) The slightly bent junction between bypass and vessel is exposed to high shear forces during the systole. The good correspondence between the static and moving vessel quantification is due to the lack of movement in the vascular prosthesis. The altered vessel geometry promotes vortex flow in the ascending aorta. (c) In contrast to the static counterpart the motion-adjusted quantification produces higher WSS in the post-stenotic vessel section than in the coarctation. This meets the physicians' expectations, since such patients have an increased risk of post-stenotic aneurysm development. A congestion of the blood is observable that causes high velocity blood flow in the stenotic vessel section. (d) WSS, induced by near-wall vortex flow, shows good correspondence in the left pulmonary artery and differs by 35% in the right pulmonary artery of the patient.

WSS values are postprocessed in the same way as the displacements using a Laplacian-like smoothing with 250 iterations and a relaxation factor of 0.01.

The adaption to the cardiac motion is achieved by using the respective deformed mesh state M_i. The normal vectors in M_i is obtained via CPU implementation of the method described in Section 5.1, paragraph Motion Visualization.

Stroke Volume: The stroke volume (SV) is the pumped blood per heartbeat. It is quantified as amount of orthogonal flow that passes a plane over the cardiac cycle:

$$\mathrm{SV} = \iiint_{x\,y\,t} \left(\vec{u_{xyt}} \cdot \vec{n}\right) \mathrm{d}t\, \mathrm{d}y\, \mathrm{d}x\,, \tag{9}$$

where $\vec{u_{xyt}}$ are the velocity vectors sampled at the corresponding positions in the plane, $\vec{n}$ is the normal vector of the $x \times y$ sized plane. Discretization in the implementation leads to the following calculation:

$$\mathrm{SV} = \Delta x \cdot \Delta y \cdot \Delta t \cdot \vec{n} \cdot \sum_{\forall x} \sum_{\forall y} S_{xy} \cdot \sum_{\forall t} \vec{u_{xyt}}$$

$$\text{with} \quad S_{xy} = \begin{cases} 1, & (x,y) \text{ inside 3D base segmentation} \\ 0, & \text{else} \end{cases} \tag{10}$$

In the dynamic counterpart the plane has a list of T normals $\vec{n_i}$, $i \in [0,\ T-1]$, $i \in \mathbb{N}$ and a time-varying size $\Delta x_i \times \Delta y_i$ per grid element. The interval Δt between two temporal positions in the dataset remains constant. Following this, the quantification has to be adjusted to:

$$\mathrm{SV} = \Delta t \cdot \sum_{\forall t} \left(\Delta x_t \cdot \Delta y_t \cdot \vec{n_t} \cdot \sum_{\forall x} \sum_{\forall y} S_{xyt} \cdot \vec{u_{xyt}} \right)$$

$$\text{with} \quad S_{xyt} = \begin{cases} 1, & (x,y,t) \text{ inside 4D vessel segmentation} \\ 0, & \text{else} \end{cases} \tag{11}$$

6 Results

We applied our method to seven anonymized datasets of the aorta and pulmonary artery that also contain parts of the left and right ventricles and atriums (for details recall Section 3.3). In the following, we present all six pathologic cases and then proceed with a discussion. The initial three-dimensional segmentations were performed in consultation with each two radiologists and cardiologists. The graph cut-assisted four-dimensional segmentation solely used the automatically specified regions inside and outside the vessel as described in Section 5.1. All results were manually validated by the experts. The cardiac motion extractions including the graph cut-based segmentation of each temporal position were performed in less than ten seconds per case, the WSS calculation in less than three seconds on an Intel i7-3930K. The

stroke volumes are quantified in below one second on a GeForce GTX 680. All presented images were directly captured from our developed software, which is used for research purposes by the clinical collaborators.

6.1 Informal Evaluation

The patients' present situations were discussed in collaboration with experts specialized on the cardiovascular system under consideration of the additional information provided by our method. In addition, the influence of the cardiac motion on the WSS and stroke volume quantification was investigated. The WSS maximum was fixed to 2.5 Pa to facilitate the comparison between different datasets. The evaluation was performed informally, i.e., the experts were not required to solve tasks.

Aneurysm with Former Coarctation: The patient's primary disease was a coarctation, which was widened via balloon dilatation. Nine years later, the suspicion for a re-coarctation led to a new examination including a 4D PC-MRI acquisition. Significant dilations of the left subclavian artery and the distal aortic arch were diagnosed. The qualitative flow analysis reveals that high velocity blood flow passes the aortic arch and impinges on the vessel wall, shown in Figure 1. A huge vortex emerges, which is present during the whole cardiac cycle. The quantification confirms the experts' assumed increased WSS in the impingement zone. They agree that the pathologic vessel dilation was most likely caused by the high shear forces for nearly a decade. A systolic vortex in the ascending aorta is probably induced by the patient's bicuspid aortic valve. The complex blood flow close to the wall causes high shear forces in this vessel section. Unlike in the impingement zone, the peak WSS values obtained with and without motion consideration differ about 25%, as depicted in Figure 8a.

Aortic Bypass with Former Coarctation: After the second patient's coarctation was widened via balloon dilatation, a re-coarctation occurred and a bypass surgery was performed. The 4D PC-MRI dataset was acquired in the postoperative examination process. Our motion extraction achieved plausible results: there is a strong movement in the aortic root, no noticeable contraction in the vascular replacement and then again a peristaltic wall motion. The quantification revealed that the slightly bent prosthesis-vessel junction is exposed to increased WSS, shown in Figure 8b. Follow-up examinations were suggested concordantly by the physicians to keep track of the potential initiation and development of a pathologic dilation in this vessel section. This way, appropriate prevention measures can be performed if necessary. The motion-adjusted quantification produces no significant WSS differences in the bypass due to the negligible movement. Solely the peak appears more prominent with motion consideration. The stroke volume quantification shows a similar behavior. In the prosthesis, there is a less than 5% motion-induced difference, whereas the values in the ascending aorta differ up to 10%.

Aneurysm, Coarctation and Insufficiency: The third patient suffers from an aneurysm in the ascending aorta and a coarctation. In addition, the improperly shutting aortic valve causes a large amount of retrograde blood flow during the diastole from the aorta back into the left ventricle. The percentaged back flow is referred to as regurgitation fraction. The stroke volume, measured directly above the aortic valve, is about 85 ml in the static vessel, the regurgitation fraction is 21%. The motion-adjusted calculation produces 7 ml less volume per heartbeat and a regurgitation fraction of 26%. There was disagreement whether a valve implantation surgery is advisable. We conclude that such deviations, especially in critical situations, may influence the assessment of the treatment urgency. Yet, the experts agreed that the patient's overall situation is crucial to determine an appropriate treatment decision.

The further analysis revealed increased shear forces in the coarctation. A pre-stenotic congestion is observable in the qualitative flow analysis during the systole. High velocity blood passes the coarctation and impinges on the wall. The post-stenotic vessel section is exposed to increased shear stress, illustrated in Figure 8c. The conventional quantification produces higher WSS values in the coarctation than in the post-stenotic vessel section. Motion consideration results in the opposite, which is more plausible according to the physicians. They explain that post-stenotic vortex flow often leads to pathologic vessel dilations in similar patients.

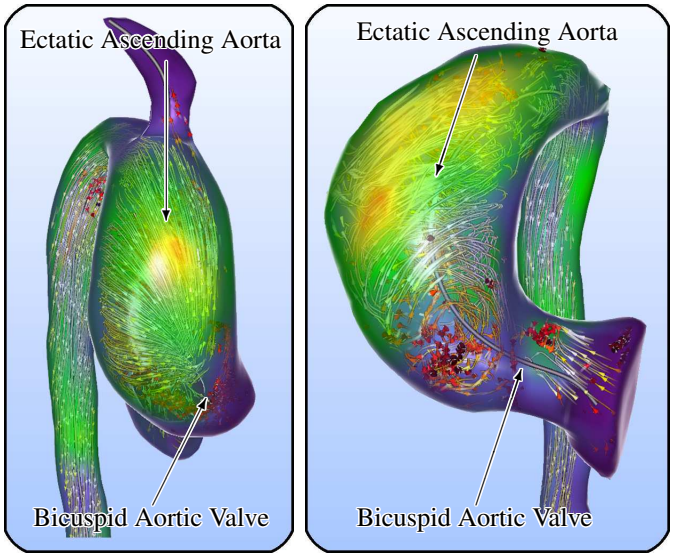

(a) (b)

Fig. 9. WSS quantification under consideration of the cardiac motion in two bicuspid aortic valve patients with integrated flow visualization. In both cases, a large systolic vortex in the ascending aorta causes increased shear forces on the already dilated vessel wall.

Pulmonary Insufficiency: An ultrasonography revealed the fourth patient's serious condition: a pulmonary insufficiency. The improperly shutting pulmonary valve is not able to prevent 30% of the blood from flowing back into the right ventricle during the diastole. The consequence are symptoms like dyspnea during physical exertion, frequently occurring palpitations and nausea. Systolic vortex flow in the right pulmonary artery is promoted by the altered valve morphology. During diastole, the retrograde flow causes turbulences of the blood. Thus, the right pulmonary artery is exposed to increased shear forces during the full cardiac cycle. The left pulmonary artery shows increased WSS solely in the systole. The peak values obtained with the conventional and motion-aware quantification show a good correspondence in the left pulmonary artery, but differ by about 35% in the right one during the systole, as shown in Figure 8d.

Bicuspid Aortic Valve with Vessel Dilation: A bicuspidality of the aortic valve promotes vortex flow in the ascending aorta in most cases [18]. If the vortex flows close to the wall with high velocities, increased shear forces are induced. As a long-term consequence, such patients often come along with a pathologic vessel dilation. Figure 9 shows two examples. The altered vessel geometry amplifies the vortex formation again, which leads to an accelerated disease progression.

Compared to the extracted motion in a healthy volunteer dataset, the vascular wall appears loose. In a resulting discussion, the physicians show great interest in possibilities to derive a wall model that includes the elasticity. The further debate is about a recently developed treatment option named transcatheter aortic valve implantation (TAVI). It is less invasive than conventional valve replacement surgeries. The feasibility of TAVIs in BAV patients is a current research topic.

The absolute WSS values and peak locations showed no significant differences with and without consideration of the vessel motion in both patients. The qualitative flow analysis indicates that this might be due to the homogeneous behavior of near-wall velocity vectors along the inward-pointing surface normals.

6.2 Discussion

The graph cut-based four-dimensional segmentation does not require the specification of any unintuitive parameters. Instead, the experts' knowledge is exploited by letting them specify regions inside and outside the vessel. The physicians appreciate the possibility to verify and adjust the three- as well as the four-dimensional segmentation at any time. However, the automatically extracted motion results were sufficiently good so that no manual correction was necessary for the presented cases. The obtained behaviors of the cardiac motions were plausible. Heavy movement was detected in ventricles as well as the aortic roots and pulmonary trunks. Periodic vessel diameter changes vividly illustrate the heart's contraction and expansion. Vessel sections with vascular replacements showed barely noticeable alterations.

The differences between the motion-adjusted and conventional WSS quantification were highest in regions of strong movement. The peak locations showed a good correspondence in most cases, but the absolute values differed up to 35%. Derived from the discussion, physicians are currently more interested in the peak locations than concrete numbers. This is due to a lack of experience with WSS quantification in 4D PC-MRI data. In addition, the degree of uncertainty caused by, e.g., low image resolution is not yet sufficiently clarified. Nevertheless, the WSS quantification in a three-dimensional vessel approximation for the sole purpose of finding peak locations can be recommended. The absolute values, however, need careful interpretation.

The conventional stroke volume quantification without motion consideration showed great sensitivity to the plane location and orientation, especially in vessel sections with vortex flow. In regions with laminar flow, the stroke volumes were more reliable with rather small deviations up to 10%. A possible explanation is as follows: The aorta and pulmonary artery have their minimal diameter in the diastole. Due to the blood that is pumped into the body, they swell to their maximum diameter during the systole. At this point, they have approximately the same size as the vessel extracted from the three-dimensional base segmentation that was performed on the magnitude tMIP. As a consequence, the difference between the conventional and motion-aware stroke volume integration is smallest at this time of the cardiac cycle. The vessels' contraction and expansion leads to the time-dependent exclusion of peripheral quantification plane regions from the movement-adjusted stroke volume calculation. In the aorta and pulmonary artery, this excluded boundary region is largest in the diastole due to the minimal diameter. Nevertheless, the error remains small because of the low diastolic blood flow velocities with little contribution to the stroke volume. During the systole, as the vessel diameter and the velocities increase, the main blood flow jet is often centrally located, as depicted in Figure 10. Following from this, the excluded peripheral plane region (illustrated as darkened border) still has limited influence on the integrated stroke volume. As an overall conclusion, the difference between the conventional and motion-aware stroke volume quantification is highest in the aorta and pulmonary artery if there is diastolic high velocity blood flow close to the vascular wall. The left and right atrium have an analogous contraction and expansion behavior, see Figure 7. In contrast, the ventricles' volumes are maximal in the diastole and minimal in the systole due to the muscle contraction that ejects the blood. Yet, a similar argumentation is applicable. In all situations, a certain deviation is additionally caused by the time-varying orientation of the motion-adjusted quantification planes since they follow the moving centerline and the stroke volume is obtained as amount of flow passing the plane orthogonally.

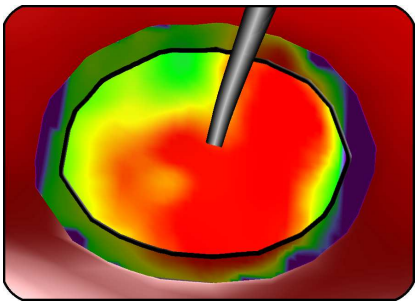

Fig. 10. The view onto a vessel's (red surrounding) cross-section with a quantification plane color-coded by velocity and orthogonal to the centerline (gray). The motion-adjusted stroke volume quantification does not consider the darkened peripheral regions when the vessel is contracted. Yet, the obtained stroke volumes via conventional and motion-aware calculation differ only slightly since the main blood flow jet with high velocities, which have the highest contribution, is located in the center.

7 Conclusion and Future Work

We have shown that our method reliably extracts plausible results for the cardiac motion. We presented a motion-adjusted quantification of vectorial WSS and stroke volume as well as the investigation of their sensitivity to the obtained movement information. In addition, we established a smooth and accurate visualization of the heart's motion with emphasis on the transition between single heartbeats. Graph cuts were employed to support segmentation tasks and showed a high level of acceptance among the consulted radiologists and cardiologists due to the intuitive interaction. The WSS peak locations showed a good correspondence with and without motion consideration, while the peak values differed up to 35%. The identification of peak locations using a static three-dimensional vessel approximation can be recommended. We found smaller deviations up to 10% in the quantified stroke volumes and provided a possible explanation. Accompanying discussions with cardiologists and radiologists revealed a primary interest in WSS peak locations. Absolute values have to be treated with caution.

The vectorial WSS is obtained as the first derivative of velocity vectors along the inward-pointing surface normal projected onto the plane orthogonal to the normal. A future work could estimate the WSS uncertainty using the second order derivatives.

Information about the cardiac motion open up multiple opportunities. The pumped blood volume in right heart insufficiencies is often higher than expected. One assumption is that this is due to a passive movement of the right ventricle caused by the left one. Next, the more accurate determination of the valve positions and orientations of the heart from 4D PC-MRI data becomes possible. Valve models facilitate the further understanding of vortex formation in, e.g., bicuspid aortic valve patients. Finally, the heart's contraction behavior allows conclusions regarding the wall elasticity, which is important for the risk assessment of aneurysm rupture and thus allows a more precise diagnosis and supports treatment decisions. The derivation of a vascular wall model was a major interest of the consulted experts.

The presented work is a contribution in the exploration of the possibilities opened up by 4D PC-MRI acquisitions. Yet, further research to validate the reliability of the obtained results and general quantification in measured data is inevitable.

In the future, standardized and (semi-)automatic evaluation methods will enable the processing of large studies that facilitate the statistical investigation of gender- and age-specific norm values. The derived normal physiological ranges of different flow parameters will support the assessment of vascular disease severity.

References

[1] A. Abufadel. *4D Segmentation of Cardiac MRI Data Using Active Surfaces with Spatiotemporal Shape Priors*. PhD thesis, Georgia Institute of Technology, 2006.

[2] T. Akenine-Möller, E. Haines, and N. Hoffman. *Real-Time Rendering 3rd Edition*. A. K. Peters, Ltd., Natick, MA, USA, 2008.

[3] L. Antiga, B. Ene-Iordache, and A. Remuzzi. Centerline Computation and Geometric Analysis of Branching Tubular Surfaces with Application to Blood Vessel Modeling. In *Proc Winter School Comput Graph (WSCG)*, 2003.

[4] M. Bertram, G. Reis, R. H. van Lengen, S. Köhn, and H. Hagen. Non-Manifold Mesh Extraction from Time-Varying Segmented Volumes used for Modeling a Human Heart. In *Proc EuroVis*, pages 199 – 206, 2005.

[5] S. Born, M. Markl, M. Gutberlet, and G. Scheuermann. Illustrative Visualization of Cardiac and Aortic Blood Flow from 4D MRI Data. In *IEEE PacificVis*, 2013.

[6] S. Born, M. Pfeifle, M. Markl, M. Gutberlet, and G. Scheuermann. Visual Analysis of Cardiac 4D MRI Blood Flow Using Line Predicates. *IEEE Trans Vis Comput Graph*, 19:900 – 912, 2013.

[7] Y. Boykov and M.-P. Jolly. Interactive Organ Segmentation Using Graph Cuts. In *Proc Med Imag Comput Comput Assist Interv*, pages 276 – 286, 2000.

[8] Y. Boykov and V. Kolmogorov. An Experimental Comparison of Min-Cut/Max-Flow Algorithms for Energy Minimization in Vision. *IEEE Trans Patt Anal Mach Intell*, 26:359 – 374, 2001.

[9] M. A. Castro, M. C. Ahumada Olivares, C. M. Putman, and J. R. Cebral. Intracranial Aneurysm Wall Motion and Wall Shear Stress from 4D Computerized Tomographic Angiography Images. *Proc Int Soc Opt Phot (SPIE)*, 8672, 2013.

[10] J. Cousty, L. Najman, M. Couprie, S. C. Guinaudeau, T. Goissen, and J. Garot. Segmentation of 4D Cardiac MRI: Automated Method based on Spatio-Temporal Watershed Cuts. *Image Vis Comput*, 28(8):1229 – 1243, 2010.

[11] C. Dìaz and L. A. Robles. Fast Noncontinuous Path Phase-Unwrapping Algorithm based on Gradients and Mask. In *Proc Iberoameric Cong Patt Recog (CIARP)*, pages 116 – 123, 2004.

[12] J. R. Dormand and P. J. Prince. A Family of Embedded Runge-Kutta Formulae. *J Comput Appl Math*, 6:19 – 26, 1980.

[13] K. D. Fritscher, R. Pilgram, and R. Schubert. Automatic Cardiac 4D Segmentation Using Level Sets. In *Proc Funct Imag Model Heart*, pages 113 – 122, 2005.

[14] R. Gasteiger, M. Neugebauer, O. Beuing, and B. Preim. The FLOWLENS: A Focus-and-Context Visualization Approach for Exploration of Blood Flow in Cerebral Aneurysms. *IEEE Trans Vis Comput Graph*, 17(12):2183 – 2192, 2011.

[15] R. Gasteiger, M. Neugebauer, C. Kubisch, and B. Preim. Adapted Surface Visualization of Cerebral Aneurysms with Embedded Blood Flow Information. In *Proc Eurographics Vis Comput Biol Med*, pages 25 – 32, 2010.

[16] J. Geiger, M. Markl, L. Herzer, D. Hirtler, F. Loeffelbein, B. Stiller, M. Langer, and R. Arnold. Aortic Flow Patterns in Patients with Marfan Syndrome Assessed by Flow-Sensitive Four-Dimensional MRI. *J Magn Reson Imag*, 35(3):594 – 600, 2012.

[17] A. Hennemuth, O. Friman, C. Schumann, J. Bock, J. Drexl, M. Huellebrand, M. Markl, and H.-O. Peitgen. Fast Interactive Exploration of 4D MRI Flow Data. *Proc Int Soc Opt Phot (SPIE)*, 7964, 2011.

[18] M. D. Hope, J. Wrenn, M. Sigovan, E. Foster, E. E. Tseng, and D. Saloner. Imaging Biomarkers of Aortic Disease - Increased Growth Rates with Eccentric Systolic Flow. *J Amer Coll Cardiol*, 60(4):356 – 357, 2012.

[19] H. Hoppe. New Quadric Metric for Simplifying Meshes with Appearance Attributes. In *Proc IEEE Vis*, pages 59 – 66, 1999.

[20] O. Jamriška, D. Sýkora, and A. Hornung. Cache-Efficient Graph Cuts on Structured Grids. In *Proc IEEE Comput Vis Patt Recog*, pages 3673 – 3680, 2012.

[21] B. Köhler, R. Gasteiger, U. Preim, H. Theisel, M. Gutberlet, and B. Preim. Semi-Automatic Vortex Extraction in 4D PC-MRI Cardiac Blood Flow Data Using Line Predicates. *IEEE Trans Vis Comput Graph*, 19(12):2773 – 2782, 2013.

[22] J.-W. Lankhaar, M. B. M. Hofman, J. T. Marcus, J. J. M. Zwanenburg, T. J. C. Faes, and A. Vonk-Noordegraaf. Correction of Phase Offset Errors in Main Pulmonary Artery Flow Quantification. *J Magn Reson Imag*, 22(1):73 – 79, 2005.

[23] J. Lantz, J. Renner, and M. Karlsson. Wall Shear Stress in a Subject Specific Human Aorta - Influence of Fluid-Structure Interaction. *Int J Appl Mech*, 3(4):759 – 778, 2011.

[24] J. Liu and J. Sun. Parallel Graph-Cuts by Adaptive Bottom-Up Merging. In *Proc IEEE Comput Vis Patt Recog*, pages 2181 – 2188, 2010.

[25] H. Lombaert, Y. Sun, and F. Cheriet. Fast 4D Segmentation of Large Datasets Using Graph Cuts. In *Proc Int Soc Opt Phot (SPIE)*, volume 7962, pages 79622H–79622H–7, 2011.

[26] J. Lotz, C. Meier, A. Leppert, and M. Galanski. Cardiovascular Flow Measurement with Phase-Contrast MR Imaging: Basic Facts and Implementation. *Radiographics*, 22(3):651 – 671, 2002.

[27] M. Mahapatra and J. M. Buhmann. Automatic Cardiac RV Segmentation Using Semantic Information with Graph Cuts. In *Proc Int Symp Biomed Imag*, pages 1106 – 1109, 2013.

[28] M. Markl, A. Frydrychowicz, S. Kozerke, M. D. Hope, and O. Wieben. 4D Flow MRI. *J Magn Reson Imag*, 36(5):1015 – 1036, 2012.

[29] T. McLoughlin, R. S. Laramee, R. Peikert, F. H. Post, and M. Chen. Over Two Decades of Integration-Based, Geometric Flow. *Comp Graph Forum*, 29(6):1807 – 1829, 2010.

[30] S. Mendis, P. Puska, and B. Norrving. *Global Atlas on Cardiovascular Disease Prevention and Control*. World Health Organization, World Heart Federation and World Stroke Organization, 2011.

[31] J. Montagnat and H. Delingette. 4D Deformable Models with Temporal Constraints: Application to 4D Cardiac Image Segmentation. *J Med Imag Analysis*, 9(1):87 – 100, 2005.

[32] M. Neugebauer, G. Janiga, O. Beuing, M. Skalej, and B. Preim. Anatomy-Guided Multi-Level Exploration of Blood Flow in Cerebral Aneurysms. *Comp Graph Forum*, 30(3):1041 – 1050, 2011.

[33] A. M. Nixon, M. Gunel, and B. E. Sumpio. The Critical Role of Hemodynamics in the Development of Cerebral Vascular Disease. *J Neurosurg*, 112(6):1240 – 1253, 2010.

[34] T. G. Papaioannou and C. Stefanadis. Vascular Wall Shear Stress: Basic Principles and Methods. *Hellenic J Cardiol*, 46(1):9 – 15, 2005.

[35] S. Petersson. *Fast and Accurate 4D Flow MRI for Cardiovascular Blood Flow Assessment*. PhD thesis, Linköping University, Division of Cardiovascular Medicine, Center for Medical Image Science and Visualization, Faculty of Health Sciences, 2013.

[36] A. Pobitzer, A. Lez, K. Matkovic, and H. Hauser. A Statistics-Based Dimension Reduction of the Space of Path Line Attributes for Interactive Visual Flow Analysis. In *Proc IEEE PacificVis*, pages 113 – 120, 2012.

[37] W. V. Potters, M. Cibis, H. A. Marquering, E. vanBavel, F. Gijsen, J. J. Wentzel, and A. J. Nederveen. 4D MRI-Based Wall Shear Stress Quantification in the Carotid Bifurcation: A Validation Study in Volunteers Using Computational Fluid Dynamics. *J Cardiovasc Magn Reson*, 16(Suppl 1):P162, 2014.

[38] W. V. Potters, P. van Ooij, E. Vanbavel, and A. Nederveen. Vectorial Wall Shear Stress Calculations in Vessel Structures Using 4D PC-MRI. *J Cardiovasc Magn Reson*, 14(1):W5, 2012.

[39] U. Preim, F. Hause, L. Lehmkuhl, B. Preim, A. Greiser, M. Grothoff, and M. Gutberlet. Comparison of 4D and 2D Phase Contrast Magnetic Resonance Imaging of the Great Mediastinal Vessels. *J Cardiovasc Magn Reson*, 15(Suppl 1):P35, 2013.

[40] W. H. Press, S. A. Teukolsky, W. T. Vetterling, and B. P. Flannery. *Numerical Recipes - The Art of Scientific Computing (Third Edition)*. Cambridge University, 2007.

[41] T. Salzbrunn, C. Garth, G. Scheuermann, and J. Meyer. Pathline Predicates and Unsteady Flow Structures. *The Visual Computer*, 24(12):1039 – 1051, 2008.

[42] G. Taubin, T. Zhang, and G. Golub. Optimal Surface Smoothing as Filter Design. In *Proc Europ Conf Comput Vis*, pages 283 – 292. 1996.

[43] P. van Ooij, W. V. Potters, A. Guédon, J. J. Schneiders, H. A. Marquering, C. B. Majoie, E. Vanbavel, and A. J. Nederveen. Wall Shear Stress Estimated with Phase Contrast MRI in an In Vitro and In Vivo Intracranial Aneurysm. *J Magn Reson Imag*, 38(4):876 – 848, 2013.

[44] P. van Ooij, W. V. Potters, A. J. Nederveen, J. D. Collins, J. C. Carr, S. C. Malaisrie, M. Markl, and A. J. Barker. Thoracic Aortic Wall Shear Stress Atlases in Patients with Bicuspid Aortic Valves. *J Cardiovasc Magn Reson*, 16(Suppl 1):P161, 2014.

[45] R. van Pelt, J. O. Bescos, M. Breeuwer, R. E. C., M. E. Gröller, B. ter Haar Romenij, and A. Vilanova. Exploration of 4D MRI Blood Flow Using Stylistic Visualization. *IEEE Trans Vis Comput Graph*, 16(6):1339 – 1347, 2010.

[46] S. Venkataraman. 4D Visualization of Cardiac Flow. NVIDIA GPU Tech Conf 2010 Talk.

[47] J. C. Yang, J. Hensley, H. Grün, and N. Thibieroz. Real-Time Concurrent Linked List Construction on the GPU. In *Proc Eurographics Symp Rend*, pages 1297 – 1304, 2010.

[48] Q. Zhang, R. Eagleson, and T. M. Peters. Dynamic Real-Time 4D Cardiac MDCT Image Display Using GPU-Accelerated Volume Rendering. *Comp Med Imag Graph*, 33(6):461 – 476, 2009.

[49] F. Zhao, H. Zhang, A. Wahle, T. D. Scholz, and M. Sonka. Automated 4D Segmentation of Aortic Magnetic Resonance Images. In *Proc Brit Mach Vis Conf*, pages 247 – 256, 2006.